PCCP

PAPER

View Article Online
View Journal | View Issue

Cite this: *Phys. Chem. Chem. Phys.*, 2025, **27**, 12069

Persistence of Ce^{3+} species on the surface of ceria during redox cycling: a modulated chemical excitation investigation†

C. Hachemi, [a] H. Dib,[b] M. Debbichi, [c] M. Badawi, [d] C. Eads,[ef] M. Ibrahim,[b] S. Loridant, [a] J. Knudsen,[ef] H. Kaper [b] and L. Cardenas [a]*

Received 3rd April 2025,
Accepted 16th May 2025

DOI: 10.1039/d5cp01283j

rsc.li/pccp

Operando resonant photoelectron spectroscopy (RPES) combined with modulated chemical excitation revealed the dynamic evolution of Ce^{3+}/Ce^{4+} redox states at the surface of CeO_2 during the CO oxidation reaction. Using alternating CO and O_2 pulses as chemically modulated signals, we monitored the surface states in the valence band region, unveiling the evolution of electronic structure during the catalytic process. The analysis with different gas flow ratios revealed that under CO-rich conditions ($CO:O_2 \geq 1$), only partial conversion from Ce^{3+} to Ce^{4+} occurred. In contrast, complete Ce^{3+} to Ce^{4+} conversion was achieved when pulsing O_2 into O_2-rich environments. Furthermore, we find that intermediate oxygen species, such as peroxo and OH, impact the conversion of Ce^{3+} and Ce^{4+}. These oxygenated species coexist between 330 °C and 360 °C in pure O_2, while above 390 °C only OH groups remain stable on the ceria surface.

Introduction

Ceria-based catalysts are of pivotal importance in many chemical processes, such as automotive exhaust treatment,[1] water gas shift,[2] and CO oxidation reactions.[3] The driving force of ceria as an oxygen-storage catalyst stems from its Ce^{3+} species, which act as an electron reservoir to enhance catalytic performance. Although it is widely accepted that Ce^{3+} is essential in triggering these reactions, the catalytic processes initiated when these species interact with reactants are poorly understood. In particular, knowledge about the nature of active intermediate species formed under reaction conditions remains limited.

The excess electron from Ce^{3+} serves as a reactive center, facilitating the activation of oxygen-containing molecules in the gas phase.[4,5] For instance, the dissociation process of O_2 has been described as electrophilic, where oxygen species sequentially accept electrons from the catalyst surface until complete reduction, following the path:[6]

$$O_2 \rightarrow (O_2)_s \rightarrow (O_2^-)_s \rightarrow (O_2^{2-})_s \rightarrow 2(O^-)_s \rightarrow 2(O^{2-})_s \rightarrow 2(O^{2-})_{Lattice}$$

In the Mars–van Krevelen (MvK) mechanism, gas-phase oxygen interactions play a fundamental role in maintaining the catalytic cycle. Initially, CO reacts with lattice oxygens (O^{2-}), creating oxygen vacancies in the CeO_2 lattice. These vacancies are subsequently replenished when gas-phase O_2 interacts with CeO_2. However, other pathways that entail the formation of intermediate oxygen species during the CO oxidation reaction may also play a major role.

These oxygen intermediates may serve as potential active species that influence the Ce^{3+}/Ce^{4+} ratio[7–9] *via* oxygen vacancy occupation. However, detecting these species remains a significant challenge in heterogeneous catalysis, primarily due to their low concentrations and short lifetimes.[10] To address this challenge, we propose an effective detection approach using temporal analysis methods, such as periodic modifications of the feed-gas composition. This methodology enables the catalyst surface to cycle through different activity phases during the catalytic reaction.

In this study, the surface of CeO_2 was brought to oscillate between two rich phases, oxidized (Ce^{4+}) and reduced (Ce^{3+}) by temporally changing the feed-gas composition between pure O_2 and CO. Using repeated gas pulses, we monitored the Ce^{3+} in the valence band while simultaneously detecting O_2 (m/z = 32)

[a] *Univ. Lyon, Université Claude Bernard-Lyon 1, CNRS, IRCELYON-UMR 5256, 2 av. A. Einstein, F-69626 Villeurbanne Cedex, France. E-mail: luis.cardenas@ircelyon.univ-lyon1.fr*
[b] *Saint Gobain Recherche Provence, 550, Ave Alphonse Jauffret, 84306 Cavaillon, France*
[c] *Université de Monastir, Faculté des Sciences de Monastir, Laboratoire de la matière condensée et nanosciences, LR11ES40, 5019 Monastir, Tunisia*
[d] *Université de Lorraine, CNRS, L2CM, F-54000 Nancy, France*
[e] *Division of Synchrotron Radiation Research, Department of Physics, Lund University, Lund, Sweden*
[f] *MAX IV Laboratory, Lund University, Lund, Sweden*

† Electronic supplementary information (ESI) available. See DOI: https://doi.org/10.1039/d5cp01283j

and CO (m/z = 28) by mass spectrometry (MS). As a selective reducing agent, CO converts Ce^{4+} to Ce^{3+}, which we detected through the Ce 4f electronic states in the valence band. We conducted synchronized measurements of Ce 4f and CO mass spectra to monitor the cyclical formation and depletion of Ce 4f during alternating exposure to O_2 (oxidizing) and CO (reducing) gases. This approach of studying catalyst response to an external chemical variable excitation is usually referred to as modulation excitation spectroscopy and has so far been used in APXPS for core-level analysis.[11–13]

Modulation excitation spectroscopy (MES) is an analytical technique that applies periodic chemical stimuli to study dynamic processes in catalytic materials.[14] The technique identifies specific spectroscopic features as reference events that can be tracked through repeated measurement cycles. After reaching a transient state, these cycles are averaged to enhance data quality. This approach enables systematic observation of active species responding to the excitation. The data can be further analyzed using phase-sensitive detection (PSD), described by:[15]

$$A_k\left(\varnothing_k^{\mathrm{PSD}}\right) = \frac{2}{T}\int_0^T A_{\mathrm{ave}} \sin\left(k\omega t + \varnothing_k^{\mathrm{PSD}}\right) \mathrm{d}t$$

The technique is particularly valuable in catalysis research, where it allows the detection of active and spectator species during catalytic reactions. In our study, we track the Ce 4f states as a reference event through synchronized measurements of valence band states and mass spectrometry data by temporally changing the feed-gas composition. The versatility of MES extends to various stimuli (temperature, light, electric field, feed-gas composition) and analytical methods (XAS, IR, XRD, Raman), making it an essential tool for studying active species and reaction mechanisms in catalytic processes.

Here, we developed a novel surface-sensitive *operando* technique that combines modulated chemical excitation with resonant photoelectron spectroscopy (RPES) to track transient catalytic species in the valence band region. This combined approach, supported by DFT calculations, enables the identification of both transient and stationary activated oxygen and ceria species on the CeO_2 surface as well as their relationship with the electronic structure. For the first time, we directly observed the oscillation of the Ce 4f states in the valence band as modulated chemical excitation drives the reversible conversion between Ce^{4+} and Ce^{3+}, highlighting the persistence of Ce^{3+} species in O_2-rich conditions.

Experimental methods

CeO_2 preparation and standard characterization

Pure cerium oxide nanoparticles were synthesized by the decomposition of cerium nitrate, as reported previously.[16] In brief, $Ce(NO_3)\cdot 6H_2O$ (AcrosOrganic, 99+%) was dissolved in isopropanol at room temperature. After complete dissolution, the solvent was removed by rotational evaporation at 44 °C until nearly complete dryness. The resulting solid was calcined following a controlled temperature program: from room temperature to 180 °C for 2 h, then sequentially to 200 °C (3 h), 220 °C (3 h), and finally to 500 °C (3 h). The obtained powder was ground into a fine powder using a mortar.

X-Ray diffraction (XRD) patterns of powdered samples were collected using a Bruker D8 Advance A25 diffractometer equipped with a Cu anode (Cu Kα: 0.154184 nm) (Fig. S1, ESI†). Raman spectroscopy measurements were performed using a Horiba labRAM HR spectrometer with laser excitation at 532 nm. The Raman spectra were acquired using a 300 lines per mm^{-1} grating at an incident nominal power of 1 mW (Fig. S2, ESI†).

Nitrogen (N_2) adsorption/desorption isotherms were measured at 77 K with a Micromeritics Tristar II 3020 instrument. Prior to each analysis, the samples were degassed under vacuum (< 5 Torr) overnight at 350 °C (Fig. S3, ESI†). Thermogravimetric analyses (TGA-MS) were recorded on a temperature range between 30 and 1000 °C with a ramp of 5 °C min^{-1} using a LabSysEvo TGA by Setaram, coupled with a Pfeiffer Omnistar GSD 320 mass spectrometer (Fig. S4, ESI†).

Modulated chemical excitation spectroscopy

Modulated chemical excitation spectroscopy experiments were performed at the SPECIES beamline of the MAX IV laboratory.[17,18] The measurements were conducted in a near-ambient pressure (NAP) cell (≈1 L) at a constant total pressure of 0.5 mbar using a SPECS Phoibos 150 NAP electron analyzer. To maximize the signal-to-noise ratio, the analyzer nozzle was positioned within a few millimeters of the sample surface.

CeO_2 powder was deposited on a silver foil by drop-casting after sonication in isopropanol to minimize charging effects.[19] The sample was mounted on a grounded stainless steel holder with a K-type thermocouple spot-welder near the sample surface. The sample holder was maintained on a vertical manipulator with the sample perpendicular to the analyzer nozzle (Fig. S5, ESI†). Prior to modulated chemical excitation measurements, the sample was oxidized in pure O_2 at 400 °C to remove surface carbon contamination.

Modulated chemical excitation spectroscopy measurements were collected at 1 Hz using a snapshot mode, where a fixed kinetic energy window was maintained without lens voltage scanning to ensure an adequate signal-to-noise ratio.[20] CO and O_2 gases were independently injected through mass flow controllers with a 40 s pulse length at constant flow rates, maintaining a total pressure in the NAP cell of 0.5 mbar. Modulated chemical excitation spectroscopy data were recorded at temperatures ranging from 330 to 420 °C (330, 360, 390, 400, and 420 °C) using a $CO:O_2$ flow ratio of 0.6 : 0.6 standard cubic centimeters per minute (sccm). Additional measurements at 420 °C were performed with $CO:O_2$ ratios of 1.2 : 0.6 and 0.6 : 2.4 sccm. Gas composition was monitored using a quadrupole mass spectrometer (Hiden HAL/3F PIC), which sampled gases through the electron analyzer's aperture near the sample surface.

XPS spectra were acquired at photon energies of 1030 eV (Ce 3d, wide scan), 590 eV (O 1s), and 390 eV (C 1s) to optimize photoionization cross-sections and enhance surface sensitivity. For valence band RPES, the photon energy was fixed at 121.2 eV (Ce^{3+}), 124.5 eV (Ce^{4+}), and 115 eV (off-resonance). The pass energy was set to 100 eV for snapshot modes and 50 eV for

standard spectrum mode. Energy calibration was performed using the quasi-metallic Ce 4f states, which cross the Fermi level in the Ce^{3+}-rich species, and the f^0 features in the Ce 3d spectra. The survey XPS spectrum of CeO_2 (Fig. S6, ESI†) was collected both at room temperature (as-received) and at 230 °C under ultrahigh vacuum (UHV) conditions prior to modulated chemical excitation spectroscopy experiments. The spectrum revealed Ce and O as the predominant elements, with minimal carbon contamination, indicating high sample purity and well-controlled synthesis conditions. Core-level spectra were fitted using Voigt functions (L/G ratio 0.3) and Shirley backgrounds in IgorPro 9 (Wavemetrics) (see Table S1, ESI†).

DFT calculations

The Vienna *Ab initio* Simulation Package[21,22] (VASP) was used to perform all the DFT calculations. The projector augmented wave (PAW) method and the Perdew–Burke–Ernzerhof (PBE) functional under the generalized gradient approximation (GGA) were used in the calculations.[23,24] For Ce and O atoms, the (5s, 5p, 6s, 4f, 5d) and (2s, 2p) states, respectively, were treated as valence with a plane-wave cutoff energy of 520 eV. We adopt a Γ-centered 12 × 12 × 1 *k*-point grid for the integration in the reciprocal space.[25] A vacuum layer of about 20 Å was used to avoid the interaction between the images of the CeO_2(111) surface. All the calculations are spin-polarized. To treat the electron–electron interaction on Ce 4f orbitals, we have adopted the GGA+*U* approach formulated by Dudarev *et al.*[26] by setting the effective Coulomb interaction U_{eff} to 5 eV, based on previous reports.[27,28] The effect of van der Waals (vdW) interactions on the adsorption of O_2 and OH on the CeO_2(111) surface was included through the dispersion correction of the DFT-D3 method of Grimme.[29] The convergence criteria for the total energy and the forces were set as 10^{-5} eV and 0.025 eV A^{-1}, respectively.

Results and discussion

For modulated excitation spectroscopy experiments on CeO_2, synchronization between reference events and gas pulses is crucial. Periodic O_2 and CO injections increase the pressure in the NAP cell while switching ceria between Ce^{4+} and Ce^{3+}-rich species, respectively. During CO pulses, the reduction of Ce^{4+} to Ce^{3+} is evidenced by the formation of localized Ce 4f states in the valence band (≈1 eV), characteristic of reduced Ce^{3+} species.[30–33] The synchronization between CO pulses and Ce 4f events was established by simultaneously monitoring the CO mass signal (m/z = 28) using mass spectrometry (MS) (Fig. S7, ESI†) and detecting the Ce 4f state in the valence band using RPES (Fig. S8, ESI†). Using the Ce 4f signal as a reference, we monitored its evolution during alternating cycles of CO and O_2 exposure.

These modulated chemical excitations were monitored by RPES using two beam resonant energies: Ce^{3+} (121.2 eV) and Ce^{4+} (124.5 eV; see Fig. S9, ESI†). The resonant mode allows us to improve the signal detection level for Ce^{3+} down to 0.1% of atomic concentration.[34] Fig. S10 (ESI†) demonstrates that RPES exhibits high selectivity to detect Ce^{3+} or Ce^{4+} species compared to conventional Ce 3d XPS measurements. The Ce 3d XPS spectra present multiplet structure and overlapping features, which make the analysis and determination of Ce^{3+} and Ce^{4+} species difficult.[33] In contrast, RPES enables direct identification of Ce^{3+} through selective resonant excitation of the Ce 4f state, allowing tracking of changes in the electronic structure and oxidation state of CeO_2.

(a) Tracking the Ce^{3+} event in a mixing flow ratio $CO:O_2 = 1$

Fig. 1 shows the modulated chemical excitation RPES spectra of ceria measured at a photon energy of 121.2 eV, which selectively enhances Ce^{3+} excitation through resonant processes. RPES spectra were collected during alternating gas pulses, where red horizontal bands indicate CO exposure and blue bands indicate O_2 exposure, with the sample maintained at (a) 330 °C, (b) 360 °C, (c) 390 °C, and (d) 420 °C. A $CO:O_2$ mixing ratio of 1 : 1 was maintained throughout the measurements. The formation of a Ce 4f state at 1.0 eV during CO pulses indicates Ce^{3+} formation, while its subsequent decrease during O_2 pulses demonstrates the conversion back to Ce^{4+}. This is demonstrated by the black oscillation in the left panels, which shows the integrated intensity of the Ce 4f state measured along the vertical black profile centered at 1.0 eV (±0.5 eV integration window). This periodic oscillation reaches its maximum amplitude during each CO pulse (red band) and decreases to a minimum when CO is switched off and O_2 is injected (blue band). Thus, the oscillation of the Ce 4f state clearly shows the transition between Ce^{3+} and Ce^{4+} species during periodic CO and O_2 pulses. Here, the population rate of Ce 4f serves as an excellent indicator to monitor the reduced Ce^{3+} form during ceria's redox cycle (Fig. S8(d), ESI†). Similarly, the impact of CO and O_2 pulses extends to deeper states of the valence band, particularly in the hybridized region where Ce 4f, Ce 5d, and O 2p orbitals coexist (between ≈2 eV and ≈6 eV). Although changes in this region suggest transitions between Ce^{3+} and Ce^{4+} species, the hybrid character of these states makes the identification of individual orbitals difficult.

Here, a key finding is the complete conversion between Ce^{3+} and Ce^{4+} species across a temperature range of 330 °C to 420 °C. This conversion is evident in the left panels, where the Ce 4f red oscillation reaches its maximum (Ce^{3+}) during CO injection and its minimum (Ce^{4+}) during O_2 injection. Furthermore, the profile exhibits a gradual increase in intensity (cps) with temperature, suggesting an enhancement of the Ce^{3+} state. During CO injection, the concentration of the Ce^{3+} species reaches its maximum intensity (cps) at 420 °C (see also Fig. S8(d), ESI†). Although the redox cycle highlights complete conversion between Ce^{3+} and Ce^{4+} species, the influence of feed-gas composition on ceria's redox reaction kinetics requires further investigation. Therefore, we study how different $CO:O_2$ mixing ratios, under both CO-rich and O_2-rich conditions, affect the rates of ceria oxidation (Ce^{4+}) and reduction (Ce^{3+}).

(b) Detection of persistent Ce^{3+} species under O_2-rich conditions

Here, modulated chemical excitation RPES experiments were carried out at various relative flowrates between reactants

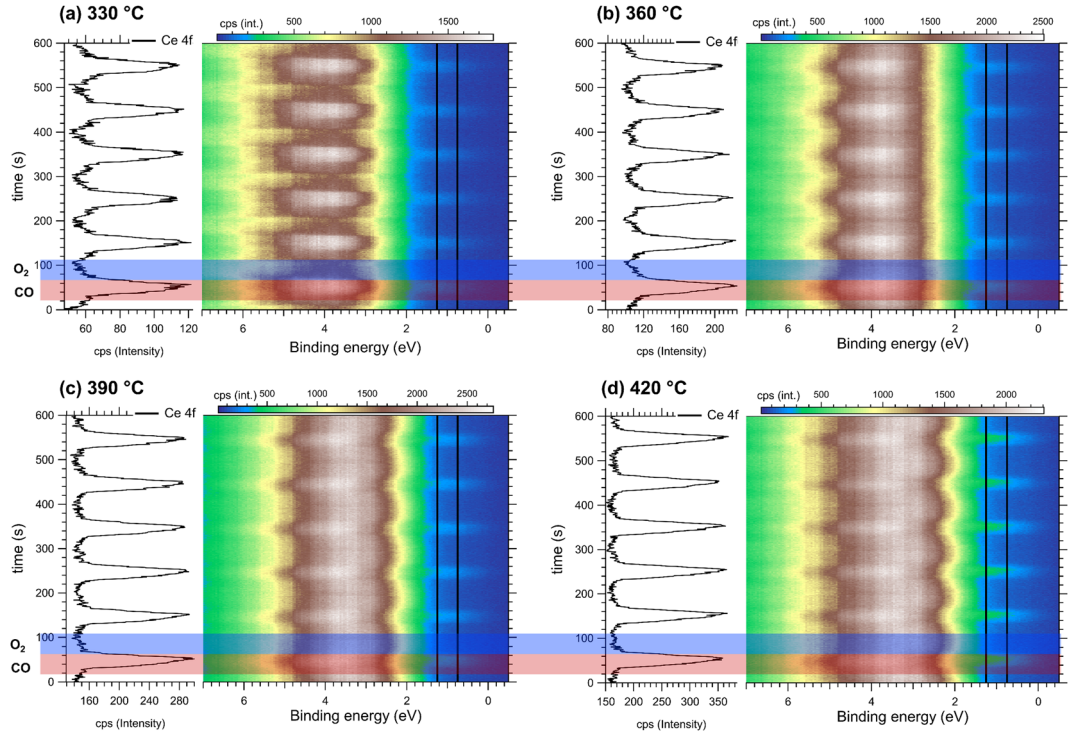

Fig. 1 Modulated chemical excitation RPES spectra showing the dynamic redox behavior of ceria. RPES spectra collected during alternating pulses of CO (red horizontal bands) and O_2 (blue horizontal bands) at (a) 330 °C, (b) 360 °C, (c) 390 °C, and (d) 420 °C, with a $CO:O_2$ mixing ratio of 1 : 1 and 40 s pulse duration. Spectra were acquired at 121.2 eV photon energy to selectively enhance Ce^{3+} detection. Left panels: Time evolution of the Ce 4f state intensity (vertical black profile centered at 1.0 ± 0.5 eV), demonstrating reversible transitions between Ce^{3+} and Ce^{4+} species during gas cycling.

with the following mixing $CO:O_2$ flow ratios: 1.2 : 0.6 sccm (Fig. 2(a)), 0.6 : 0.6 sccm (Fig. 2(b)), and 0.6 : 2.4 sccm (Fig. 2(c)). The periodic CO and O_2 pulses were synchronized with RPES spectra using mass spectrometry signals from O_2 (m/z = 32) and CO (m/z = 28) while RPES spectra were scanned. Using this synchronization protocol, we aligned the Ce 4f state in the valence band with the CO mass signal pulse (m/z = 28) (see Fig. S7 and S8, ESI†). The synchronized MS signals at the bottom of Fig. 2 (left panel) – CO (black-dotted), O_2 (blue-dotted), and CO_2 (brown-line) – reveal the correlation between gas reactivity and Ce^{3+} population states at different $CO:O_2$ ratios. The MS data shows that alternating O_2 and CO injections induce reversible transitions between Ce^{3+} and Ce^{4+} species throughout the reaction cycle.

(i) CO-rich ($CO:O_2$ = 2) conditions: Fig. 2(a) shows the electronic structure evolution of CeO_2 at 420 °C under alternating O_2 (blue band) and CO (yellow band) pulses, applied every 40 s with a CO-rich flow mixing ratio of $CO:O_2$ = 2. The corresponding MS data is shown at the bottom in the left panel of Fig. 2(d). The MS data reveal CO_2 formation when CO and O_2 reactants coexist (brown line (d)), confirming CO oxidation at 420 °C. Additionally, by varying the flow ratios, we identified the impact of reactant concentrations on CO_2 formation, as clearly evidenced by the double-peak in the CO_2 MS signal in Fig. 2(f). Here, the enhancement of the Ce 4f state at 1.0 eV correlates with CO pulses, as shown by the MS data and RPES spectra.

In contrast, during O_2 pulses a residual spectral weight persists, as pointed out by the white arrow. To analyze the distinctive features of Ce 4f during each injection, we applied a normalization procedure (detailed in Fig. S11, ESI†). Fig. 2(d) shows the normalized data with two vertical line profiles at energies of 1.0 ± 0.5 eV (blue) and 1.7 ± 0.5 eV (red), with their corresponding intensities displayed in the left panel. The phase shift between these oscillations was used to track the Ce^{3+} features at 1.0 eV and 1.7 eV. During O_2 pulsing (blue band), the oscillation at 1.7 eV reaches its maximum while the 1.0 eV signal diminishes, demonstrating a clear phase shift between these features. During CO pulses (yellow band), both oscillations reach their maxima simultaneously, showing in-phase behavior. Under pure O_2 conditions (blue band), although the complete oxidation of Ce^{3+} to Ce^{4+} should theoretically eliminate the Ce 4f signal, a detectable Ce 4f feature nevertheless persists at 1.7 eV. This result suggests that some Ce^{3+} species persist despite the oxidizing nature of O_2 pulses. This behavior continues throughout the entire 1300-second sequence of redox injection cycles (Fig. S9, ESI†), indicating a fundamental limitation in achieving complete conversion from Ce^{3+} to Ce^{4+} during the oxidation process.

RPES measurements at Ce^{3+} (121.2 eV) and Ce^{4+} (124.5 eV) threshold energies reveal the intricate interplay between O 2p–Ce 4f covalent and ionic interactions. For instance, RPES selectively probes Ce^{3+} ions through an intra-atomic process that significantly enhances the spectral intensity of pure f–f electrons, enabling the detection of these species at extremely low concentrations:

$$\text{Ce } 4d^{10}4f^{1}\text{O } 2p^{6} + h\nu \rightarrow \text{Ce } 4d^{9}4f^{2}\text{O } 2p^{6} \rightarrow \text{Ce } 4d^{10}4f^{0}\text{O } 2p^{6} + e^{-}$$

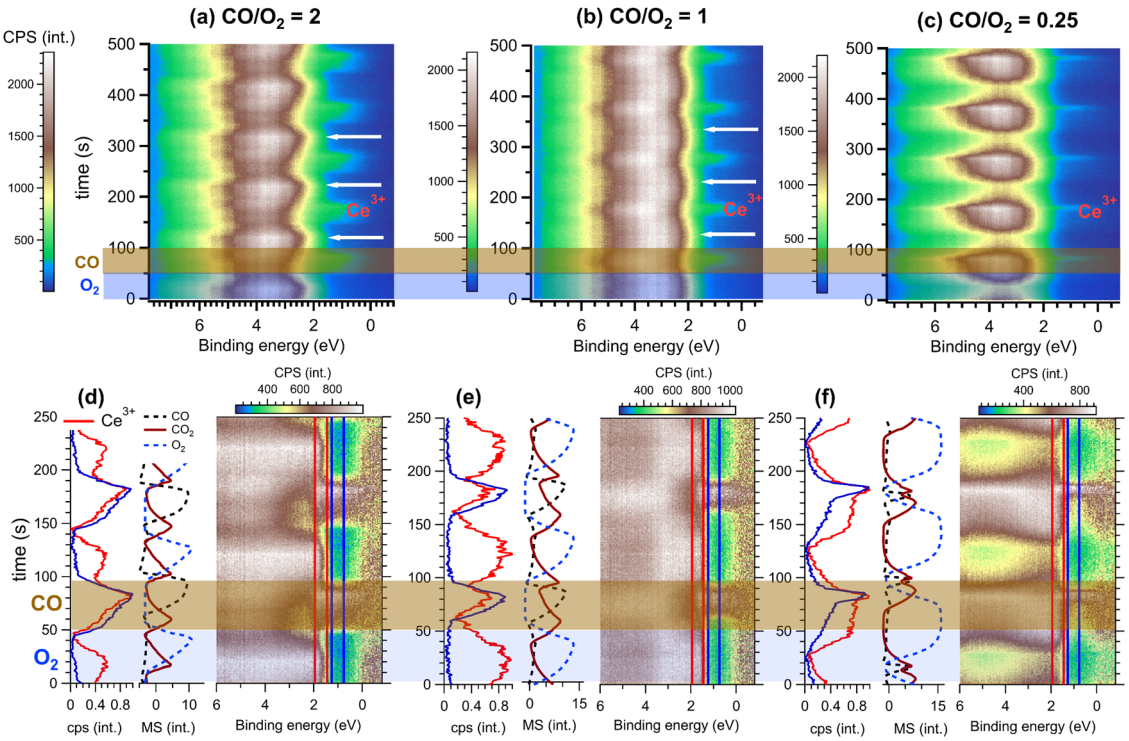

Fig. 2 On top (a), (b), and (c): Modulated chemical excitation RPES spectra measured while O_2 (blue band) and CO (yellow band) are pulsed with mixing CO/O_2 flow ratios of 2 (a), 1 (b), and 0.25 (c). The experiments were performed while ceria was kept at 420 °C. The pulse duration of each gas was 40 s. RPES spectra were obtained at the threshold energies corresponding to 121.2 eV (excitation energy for Ce^{3+}). On bottom (d), (e), and (f): RPES spectra were normalized to the highest point in the image, providing a distribution of intensities revealing regions with high spectral weight while other ones are empty. Two vertical profiles are centered at BE = 1 eV (blue) and BE = 1.7 eV (red). The left panels show CPS intensities associated with red and blue profiles, demonstrating both oscillations during CO and O_2 injections, as revealed by MS on the bottom: CO (black-dotted), O_2 (blue-dotted), and CO_2 (brown line). The white arrow points out the persistent Ce^{3+} state at the top.

In contrast, for a Ce^{4+} ion, the process is inter-atomic, providing insights into the covalent interactions between cations and anions:[35]

$$Ce\ 4d^{10}4f^{0}O\ 2p^{6} + h\nu \rightarrow Ce\ 4d^{9}4f^{1}O\ 2p^{6} \rightarrow Ce\ 4d^{10}4f^{0}O\ 2p^{5} + e^{-}$$

Analysis of modulated chemical excitation RPES data and time-constant profiles under CO and O_2 injections (Fig. S12(a) and (b), ESI†) reveals selective enhancement of Ce^{3+} (121.2 eV, top panel (a)) and Ce^{4+} (124.5 eV, bottom panel (a)) signals when using a CO-rich flow gas mixture ($CO:O_2 = 2$). During O_2 injection, the time-constant profile shifts to lower binding energies (blue line, upper panel of Fig. S12b, ESI†), appearing as a distinctive "V-shaped" electron density feature in the RPES spectrum (dashed blue line, upper panel of Fig. S12a, ESI†). The observed energy shift suggests a lattice contraction resulting from changes in oxygen stoichiometry.[36] While this shift may reflect changes in the Ce^{3+} electron population, it can also be attributed to enhanced Ce^{4+}–O 2p covalent bonding during O_2 injection at this energy.[35] RPES measurements at the Ce 4d → 4f photoabsorption threshold (121.2 eV) reveal electronic interactions more complex than simple Ce^{4+}–O 2p orbital hybridization or pure f–f electron transitions.

Furthermore, the observation of distinct Ce^{3+} states at ≈1.7 eV and ≈1.0 eV suggests implications between Ce^{3+} species and catalytic properties across different crystallographic surfaces. Recent studies demonstrate that ceria's surface morphology fundamentally controls the formation and stability of single-atom catalysts (SACs).[37,38] The exposed surface facet governs oxygen vacancy formation, which in turn determines substrate adsorption strength and catalytic activity.[39] This surface-dependent behavior manifests differently across crystallographic surfaces. For instance, the $CeO_2(100)$ surface has been shown to be catalytically active and less stable than the (111) surface,[40] making it more reactive and easily reduced under CO exposure. Similar surface-dependent behavior has been observed in H_2 reactions with CeO_2.[41]

$Pd/CeO_2(100)$ achieves exceptional selectivity (90.3%) for N alkylation reactions, performing 2.8 times better than $Pd/CeO_2(111)$.[42] A study of Au SACs shows that (110) and (111) surfaces stabilize single Au atoms in various morphologies, while the (100) surface leads to Au nanoparticle formation.[39] These differences in metal dispersion and oxygen vacancy distribution demonstrate how crystallographic structure controls both Ce^{3+} persistence and catalytic activity, making facet control a key strategy for catalyst optimization.

(ii) $CO:O_2 = 1$ flow ratio conditions: here, we used a flow of 0.6 sccm per gas, resulting in a mixing flow ratio $CO:O_2 = 1$ with a pulse length of 40 s. In Fig. 2(b), we observed the same layout describing the cycling between Ce^{3+} and Ce^{4+} rich-species as CO or O_2 are injected.

To analyze the spectral weight at 1.7 eV (white arrow) during the O_2 pulse, we applied the same analysis protocol to the normalized data in Fig. 2(e). Vertical line profiles were centered at the same energies as in Fig. 2(a): 1.0 ± 0.5 eV (blue) and 1.7 ± 0.5 eV (red). Here, both profiles exhibit behavior similar to the CO : O_2 = 2 conditions, where CO pulses generate Ce 4f states at 1.0 eV and 1.7 eV. The CO pulse drives the Ce^{4+} to Ce^{3+} conversion, evidenced by the formation of Ce 4f states. The Ce 4f character is observed at ≈1 eV and in the hybridized region between ≈3 eV and ≈6 eV,[35] demonstrating significant f-orbital contribution. During O_2 pulses, the phase shift is again observed between red and blue oscillations in the left panel, confirming the persistent reduced Ce^{3+} species. Additionally, a spectral weight between ≈2 eV and ≈6 eV in the normalized image allows us to speculate about the extension of Ce 4f in the hybridized region. These features highlight the persistence of the Ce^{3+} during O_2 pulses.

(iii) O_2-rich (CO : O_2 = 0.25) conditions: modulated chemical excitation RPES experiments were performed with alternating gas flows of O_2 = 2.4 sccm and CO = 0.6 sccm, creating O_2-rich conditions. Analysis of Fig. 2(c) shows the reversible switching between $Ce^{3+} \leftrightharpoons Ce^{4+}$ species during O_2 (blue band) and CO (yellow band) pulses. The Ce 4f state formation at ≈1 eV during CO pulses is less intense compared to conditions with CO : O_2 ratios of 2 and 1, which can be attributed to the abundance of remaining O_2.

Under O_2 pulsing, the Ce 4f state disappears, indicating a complete conversion of Ce^{3+} to Ce^{4+}. The normalized data in Fig. 2(f) confirm this through the in-phase behavior of blue and red oscillations as shown in the left panel. Both oscillations reach their maximum during CO pulsing while becoming undetectable at 1.7 eV during O_2 injections. Additionally, the Ce 4f density of states is absent between ≈2 and ≈6 eV, confirming the complete conversion of Ce^{3+} species to Ce^{4+} under O_2-rich conditions.

The MS signals (Fig. 2, bottom panels d, e, f) show the CO_2 formation across all reactant ratios. The time intervals between CO_2 peaks vary with the CO : O_2 ratio: with intervals of 40, 22, and 11 seconds observed for ratios of 2, 1, and 0.25, respectively. As the CO : O_2 ratio decreases to 0.25, the two CO_2 peaks gradually merge into a near-single peak, indicating a decline in the CO_2 production. Under O_2-rich conditions, the extended O_2 residence time promotes the formation of active oxygen and Ce^{4+} species at the surface of ceria. Consequently, the sustained CO_2 production in these conditions, despite low Ce^{3+} concentration, suggests synergistic activity between activated oxygen (Ce^{4+}–O 2p) and Ce^{3+} species.

A key objective of this study is to characterize surface oxygen species and their binding interactions with Ce^{3+} and Ce^{4+} sites. Using NAP-XPS and NAP-RPES under pure O_2 steady-state conditions, we investigate oxygen speciation at the ceria surface and its interaction with Ce^{3+} cations.

(c) Identification of surface-active oxygen species on CeO_2

Here, we combine NAP-XPS and NAP-RPES under steady-state O_2 gas flow to identify oxygen species formed at the ceria

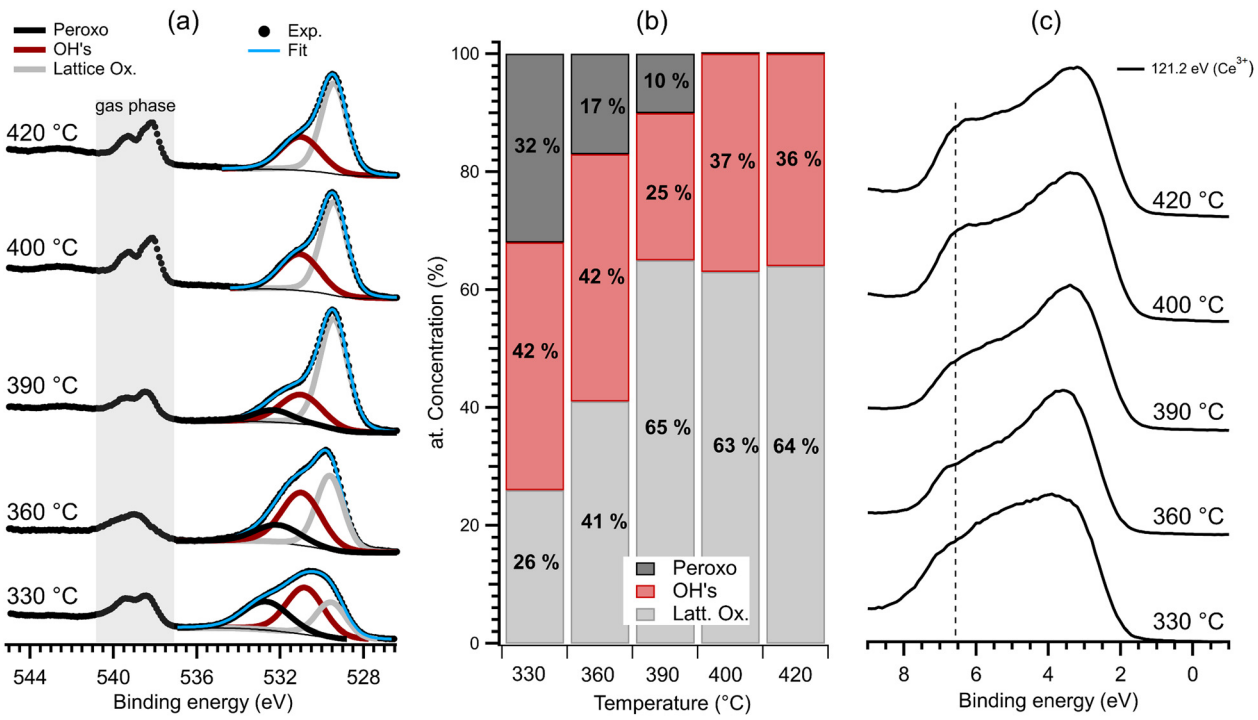

Fig. 3 Chemical species evolution and electronic states of ceria were characterized by: (a) NAP-XPS, (b) quantitative analysis showing the temperature-dependent relative concentrations of observed species, and (c) NAP-RPES spectroscopy. O 1s core level spectra were collected using 590 eV photon energy, and resonant photoemission spectra were acquired at 121.2 eV (Ce^{3+} resonance). Measurements were conducted under 0.5 mbar of O_2 at increasing temperatures from bottom to top: 330 °C, 360 °C, 390 °C, 400 °C, and 420 °C. The feature at ≈6.5 eV (dashed line) corresponds to hydroxyl groups.

surface and to investigate their interactions with Ce^{3+} species. Fig. 3(a) shows the O 1s core level spectra obtained at 590 eV of photon energy, with ceria exposed to 0.5 mbar of O_2 at constant temperatures of 330 °C, 360 °C, 390 °C, 400 °C and 420 °C, respectively. The O 1s spectra show contributions attributed to ceria lattice oxygen (529.5 eV),[43] hydroxyls (531.0 eV)[44,45] peroxide-like oxygen groups,[46,47] (532.7 eV), and O_2 gas phase (gray band).[48] The fitting at 330 °C revealed 26% of lattice oxygen, 42% of hydroxyl groups, and 32% of peroxide species. However, as shown in Fig. 3(b) a substantial evolution of all species is observed between 330 °C and 420 °C, with a marked decrease of OH and peroxo groups between 360 °C and 390 °C, while the concentration of lattice oxygen species gradually increases. From 400 °C, the peroxo contribution disappears while hydroxyl species reach a concentration of 37% constant between 400 °C and 420 °C. Thus, above 400 °C only ceria lattice oxygen and OH species remain on the CeO_2 surface (see Table S1 for more details, ESI†).

The NAP-XPS results were then contrasted with the NAP-RPES valence band analysis. Fig. 3(c) shows the NAP-RPES spectra measured at 121.2 eV (Ce^{3+}) using the same experimental temperature and gas pressure conditions as those of the NAP-XPS analysis. Here, NAP-RPES was unable to detect Ce^{3+} species ($\approx$1 eV) despite its extreme sensitivity (down to 0.1%).[34] The absence of Ce^{3+} can be attributed to their short lifetime, which renders them undetectable within the steady-state regime.[10] However, the valence band clearly shows the formation of a shoulder at $\approx$6.5 eV (dashed line), which has been attributed to OH groups by XPS, RPES, and DFT calculations.[44,45,49] Thus, this state (dashed line) confirms the attribution of OH contribution detected here by NAP-XPS. Therefore, our steady-state NAP-RPES and NAP-XPS measurements are mutually consistent, revealing that the redox cycle involves the OH species at all temperatures, while peroxo participates only between 330 °C and 390 °C. In the following section, we used DFT calculations to support the findings observed in the valence band.

(d) DFT modeling of CeO_2 surface

DFT calculations were performed to evaluate the impact of superoxo, peroxo, and OH species on the density of states (DOS) at the ceria surface. Our work focused on the CeO_2(111) surface due to its high catalytic activity and low surface energy compared to other surfaces. We further verified its stability by calculating surface energies, which provide insights into the stabilities of surfaces. A lower surface energy corresponds to a more stable surface. The calculated surface energies for the (111) and (100) surfaces are 0.421 and 0.795 eV $Å^{-2}$, respectively, indicating that the (111) face is indeed the more stable surface. Fig. S16 (ESI†) shows an oxygen vacancy (V_o) on the (100) surface with the corresponding PDOS.

Fig. 4 shows the structural models of (a) pristine CeO_2(111), (b) a defective CeO_2 surface with oxygen vacancies (V_0), and the corresponding DOS after adsorption of (c) superoxo, (d) peroxo, and hydroxide species in (e) bridge and (f) top configurations, where the DOS is compared with RPES experimental results. A Gaussian broadening of 0.2 eV was applied to all projected density of states (PDOS) to match the bandwidth observed in the experimental RPES data.

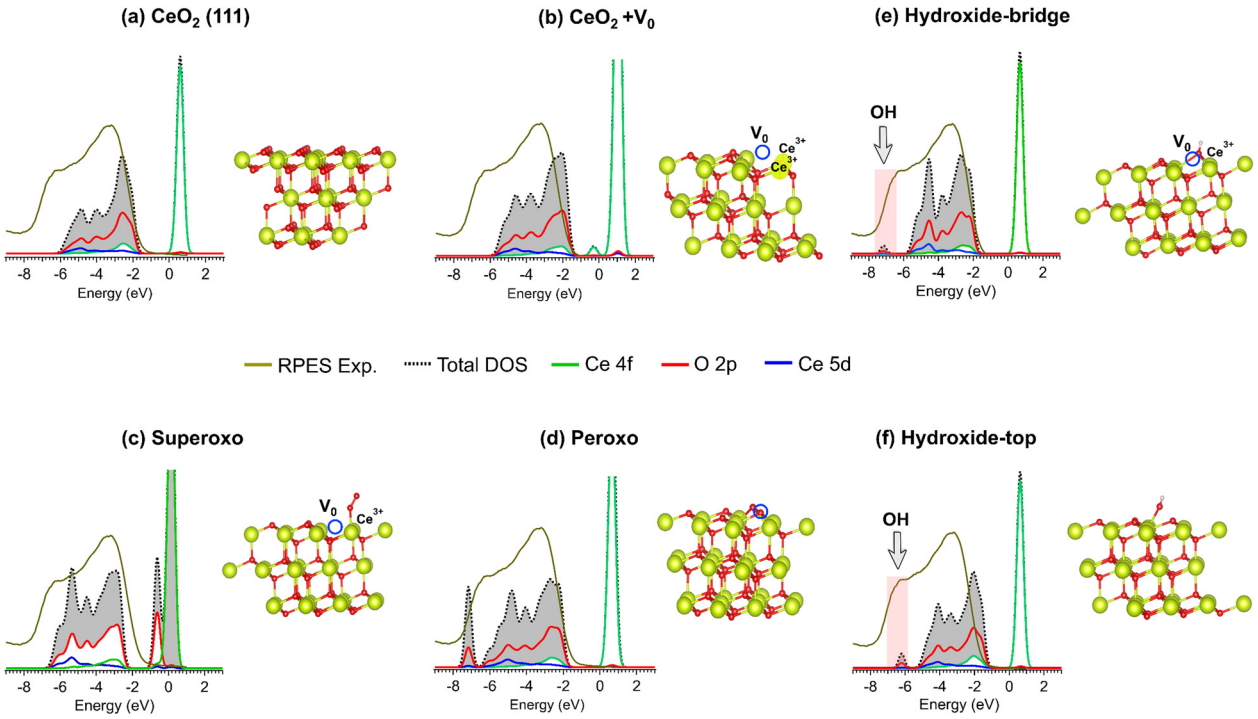

Fig. 4 Comparison of DFT calculations and RPES measurements (under 0.5 mbar O_2 at 420 °C). (a)–(f) PDOS and total DOS calculations for: (a) pristine CeO_2(111), (b) CeO_2(111) with oxygen vacancy (V_o), and different oxygen species: (c) superoxo, (d) peroxo, and OH groups in (e) bridge and (f) on-top configurations. DOS calculations include contributions from Ce 4f, Ce 5d, and O 2p states. Atomic structures show Ce^{4+} cations (yellow), oxygen atoms (red), oxygen vacancy (blue), and Ce^{3+} cations. RPES measurements reveal a characteristic feature at $\approx$6.5 eV corresponding to hydroxyl groups, validating the DFT predictions.

On $CeO_2(111)$ and $CeO_2(111) + V_o$, we find that the total DOS (dashed line) in the occupied region is mainly formed by hybridized covalent O 2p and Ce 4f.[35] For $CeO_2(111)$ in the stoichiometric form (a), Ce 4f state is absent in the intragap region, while for $CeO_2(111) + V_o$ (b) the emergence of localized Ce 4f occurs as expected.[50] Ce 4f state is obtained at a V_o concentration corresponding to 1/12 atoms established in the $CeO_2(111)$ 2×2 unit cell with 12 atoms of cerium and 24 of oxygen. Likewise, the calculated bandgaps were 2.25 eV and 0.89 eV for $CeO_2(111)$ and $CeO_2(111) + V_o$, respectively, being both indirect gaps.[30]

In Fig. 4(c)–(f), we considered the three most common adsorbed oxygen species on ceria corresponding to: (c) superoxide (O_2^-), (d) peroxide (O_2^{2-}), and (e) hydroxyl species (OH). The method, geometrical parameters, Bader charges, magnetic moment, and gap energies are available in Table S2 (ESI†). Here, Fig. 4(c) reveals the surface chemistry of superoxo (O_2^-) species adsorbed on $CeO_2(111) + V_o$. The formation of an oxygen vacancy results in two electrons localizing on adjacent Ce atoms. Upon oxygen adsorption at this site, one electron transfers to form a superoxo species. This electron transfer mechanism leads to a final electronic structure containing a single Ce^{3+} center, characterized by a Ce 4f state and an electronic gap of 1.45 eV. Previous studies have reported that the stability of superoxo species from 200 °C is compromised.[51,52] In addition, it has been suggested that superoxo species can easily transform into peroxide species at high temperatures. Moreover, the RPES data do not support the presence of superoxo, as the experimental spectrum shows a state at approximately 6.5 eV that is not predicted by the DFT calculations, while the Ce 4f state predicted by DFT is not observed in the RPES data. These findings, together with the instability of superoxo species at temperatures above 330 °C, exclude the presence of superoxo on ceria under such conditions.

Fig. 4(d): DFT on $O_2^{2-}/CeO_2(111) + V_o$. Here, peroxide species replace V_o and induce a new extra state at ≈ -7.0 eV attributed to O 2p orbitals, while the Ce 4f state is absent and a wide gap of 1.87 eV is formed. The depopulation of the Ce 4f occupied state is due to the substitution of the V_o site by the peroxo groups. The stability of this group and the O 2p orbitals formation is consistent with RPES spectrum, and the peroxo evolution observed by NAP-XPS, which allows us to speculate that peroxo species can be active species between 330 °C and 360 °C.

Fig. 4(e): DFT on $OH/CeO_2(111)$. The calculations were performed following two OH adsorption models. (i) Bridge: OH molecule adsorbs at the oxygen vacancy site (V_o) on the $CeO_2(111)$ (e). (ii) Top: in this configuration, the OH molecule is adsorbed on top of a Ce^{4+} cation without oxygen vacancy (f). Both structures exhibit different energy gaps (E_g), with 2.34 eV for the bridge and 1.72 eV for the on-top configuration, respectively. Likewise, the O 2p state localized at ≈ 6.6 eV fits well with the state observed in RPES (see arrow in Fig. 4e and f). However, the stability of both OH configurations is strongly temperature dependent.[53] As evidenced in Fig. 3, the evolution of OH contribution decreases between 330 °C and 360 °C, while it remains constant between 400 and 420 °C. Thus, although NAP-XPS cannot distinguish between the top and bridging electron configurations, this reveals that OH groups are formed and dehydroxylate at different temperature ranges, which may provide valuable information about their stability.

Finally, DFT and NAP-XPS/RPES experiments show that between 330 °C and 390 °C, both peroxo and OH species coexist, and above 390 °C, only the OH species remain on the surface. Therefore, it is clear that the activation of O_2 to form a particular oxygen species is a temperature-dependent process with high affinity here to form OH species at the surface of CeO_2.

Conclusion

Through combined modulated chemical excitation investigation and DFT calculations, we characterized the dynamics of oxygen species on the ceria surface. Our findings revealed distinct temperature-dependent behavior: Ce^{3+} species persist at 420 °C under CO-rich and $CO/O_2 = 1$ conditions, while O_2-rich environments promote complete Ce^{3+} to Ce^{4+} conversion. We identified temperature-specific surface species, with OH and peroxo groups coexisting between 330–390 °C, and exclusively OH species above 390 °C.

Our modulated chemical excitation RPES approach provided valuable insights into how changes in gas composition affect the electronic structure of the CeO_2 surface. This methodology opens up new avenues for studying catalyst behavior under dynamic conditions. Future research should focus on more complex systems, particularly Pt/CeO_2, which demonstrates promising CO oxidation activity at low temperatures.

Abbreviations

RPES	Resonant photoelectron spectroscopy
NAP	Near-ambient pressure
XPS	X-Ray photoelectron spectroscopy
MvK	Mars–van Krevelen
MS	Mass spectrometry
APCell	Ambient pressure cell
MES	Modulation excitation spectroscopy

Author contributions

L. C.: conceptualization, data curation, formal analysis, visualization, supervision, project administration, methodology, investigation, funding acquisition, writing & editing the original draft. H. K., H. D. & M. I.: synthesis of catalysts & editing the original draft. J. K. & C. E.: data curation, editing the original draft. C. H.: data curation & editing the original draft. M. D. & M. B.: DFT calculations & editing the original draft. S. L.: data curation & editing the original draft.

Data availability

The supporting data in this work are presented in the paper and/or the ESI.† Source data are available from the corresponding author upon request.

Conflicts of interest

There are no conflicts to declare.

Acknowledgements

We acknowledge MAX IV Laboratory for time on Beamline SPECIES under Proposal 20220419. Research conducted at MAX IV, a Swedish national user facility, is supported by the Swedish Research Council under contract 2018-07152, the Swedish Governmental Agency for Innovation Systems under contract 2018-04969, and Formas under contract 2019-02496. We thank the following funding sources for this project: The LABEX iMUST of the University of Lyon (PINCELL: ANR-10-LABX-0064) and ANR-NACELL (Project-ANR-22-CE42-0011), created within the ''Plan France 2030'' set up by the French government and managed by the French National Research Agency. C. H. acknowledges financial support by a PhD fellowship from the French Ministry of Education. J. K. acknowledges financial support from the Swedish Research Council, grant number 2022-04363, and from the Crafoord Foundation. This work was granted access to the HPC resources of TGCC under the allocation 2023-A0140810433 made by GENCI. H. D. and H. K. also gratefully acknowledge the French National Agency for Research (ANR, Menihr Project, ref. ANR-21-CE08-0028).

References

1 J. Kašpar, P. Fornasiero and M. Graziani, Use of CeO_2-based oxides in the three-way catalysis, *Catal. Today*, 1999, **50**, 285–298.
2 Q. Fu, H. Saltsburg and M. Flytzani-Stephanopoulos, Active Nonmetallic Au and Pt Species on Ceria-Based Water-Gas Shift Catalysts, *Science*, 2003, **301**, 935–938.
3 F. C. Meunier, L. Cardenas, H. Kaper, B. Šmíd, M. Vorokhta, R. Grosjean, D. Aubert, K. Dembélé and T. Lunkenbein, Synergy between Metallic and Oxidized Pt Sites Unravelled during Room Temperature CO Oxidation on Pt/Ceria, *Angew. Chem., Int. Ed.*, 2021, **60**, 3799–3805.
4 O. V. Safonova, A. Guda, Y. Rusalev, R. Kopelent, G. Smolentsev, W. Y. Teoh, J. A. van Bokhoven and M. Nachtegaal, Elucidating the Oxygen Activation Mechanism on Ceria-Supported Copper-Oxo Species Using Time-Resolved X-ray Absorption Spectroscopy, *ACS Catal.*, 2020, **10**, 4692–4701.
5 C. Yang, X. Yu, S. Heißler, P. G. Weidler, A. Nefedov, Y. Wang, C. Wöll, T. Kropp, J. Paier and J. Sauer, O_2 Activation on Ceria Catalysts—The Importance of Substrate Crystallographic Orientation, *Angew. Chem., Int. Ed.*, 2017, **56**, 16399–16404.
6 G. Panov, K. Dubkov and E. Starokon, Active oxygen in selective oxidation catalysis, *Catal. Today*, 2006, **117**, 148–155.
7 G. Preda, A. Migani, K. M. Neyman, S. T. Bromley, F. Illas and G. Pacchioni, Formation of Superoxide Anions on Ceria Nanoparticles by Interaction of Molecular Oxygen with Ce^{3+} Sites, *J. Phys. Chem. C*, 2011, **115**, 5817–5822.
8 C. Li, K. Domen, K. Maruya and T. Onishi, Dioxygen adsorption on well-outgassed and partially reduced cerium oxide studied by FT-IR, *J. Am. Chem. Soc.*, 1989, **111**, 7683–7687.
9 C. Li, K. Domen, K.-I. Maruya and T. Onishi, Oxygen exchange reactions over cerium oxide: An FT-IR study, *J. Catal.*, 1990, **123**, 436–442.
10 R. Kopelent, J. A. van Bokhoven, J. Szlachetko, J. Edebeli, C. Paun, M. Nachtegaal and O. V. Safonova, Catalytically Active and Spectator Ce^{3+} in Ceria-Supported Metal Catalysts, *Angew. Chem., Int. Ed.*, 2015, **54**, 8728–8731.
11 A. Shavorskiy, E. Kokkonen, E. Redekop, G. D'Acunto, J. Schnadt and J. Knudsen, Time-Resolved APXPS with Chemical Potential Perturbations: Recent Developments at the MAX IV Laboratory, *Synchrotron Radiat. News*, 2022, **35**, 4–10.
12 J. Knudsen, T. Gallo, V. Boix, M. D. Strømsheim, G. D'Acunto, C. Goodwin, H. Wallander, S. Zhu, M. Soldemo, P. Lömker, F. Cavalca, M. Scardamaglia, D. Degerman, A. Nilsson, P. Amann, A. Shavorskiy and J. Schnadt, Stroboscopic *operando* spectroscopy of the dynamics in heterogeneous catalysis by event-averaging, *Nat. Commun.*, 2021, **12**, 6117.
13 M. Roger, L. Artiglia, A. Boucly, F. Buttignol, M. Agote-Arán, J. A. van Bokhoven, O. Kröcher and D. Ferri, Improving time-resolution and sensitivity of in situ X-ray photoelectron spectroscopy of a powder catalyst by modulated excitation, *Chem. Sci.*, 2023, **14**, 7482–7491, DOI: 10.1039/D3SC01274C.
14 J. Weyel, L. Schumacher, M. Ziemba, M. Pfeiffer and C. Hess, Modulation Excitation Spectroscopy: A Powerful Tool to Elucidate Active Species and Sites in Catalytic Reactions, *Acc. Chem. Res.*, 2024, **57**, 2643–2652.
15 A. Urakawa, D. Ferri and R. J. G. Nuguid, in *Springer Handbook of Advanced Catalyst Characterization*, ed. I. E. Wachs and M. A. Bañares, Springer International Publishing, Cham, 2023, pp. 967–977.
16 S. Gatla, D. Aubert, G. Agostini, O. Mathon, S. Pascarelli, T. Lunkenbein, M. G. Willinger and H. Kaper, Room-Temperature CO Oxidation Catalyst: Low-Temperature Metal–Support Interaction between Platinum Nanoparticles and Nanosized Ceria, *ACS Catal.*, 2016, **6**, 6151–6155.
17 S. Urpelainen, C. Såthe, W. Grizolli, M. Agåker, A. R. Head, M. Andersson, S.-W. Huang, B. N. Jensen, E. Wallén, H. Tarawneh, R. Sankari, R. Nyholm, M. Lindberg, P. Sjöblom, N. Johansson, B. N. Reinecke, M. A. Arman, L. R. Merte, J. Knudsen, J. Schnadt, J. N. Andersen and F. Hennies, The SPECIES beamline at the MAX IV Laboratory: a facility for soft X-ray RIXS and APXPS, *J. Synchrotron Radiat.*, 2017, **24**, 344–353.
18 E. Kokkonen, F. Lopes da Silva, M.-H. Mikkelã, N. Johansson, S.-W. Huang, J.-M. Lee, M. Andersson, A. Bartalesi, B. N. Reinecke, K. Handrup, H. Tarawneh, R. Sankari, J. Knudsen, J. Schnadt, C. Såthe and S. Urpelainen, Upgrade of the SPECIES beamline at the MAX IV Laboratory, *J. Synchrotron Radiat.*, 2021, **28**, 588–601.
19 C. Maheu, L. Cardenas, E. Puzenat, P. Afanasiev and C. Geantet, UPS and UV spectroscopies combined to position the energy levels of TiO_2 anatase and rutile nanopowders, *Phys. Chem. Chem. Phys.*, 2018, **20**, 25629–25637.

20 S. Neppl and O. Gessner, Time-resolved X-ray photoelectron spectroscopy techniques for the study of interfacial charge dynamics, *J. Electron Spectrosc. Relat. Phenom.*, 2015, **200**, 64–77.
21 G. Kresse and J. Furthmüller, Efficiency of ab-initio total energy calculations for metals and semiconductors using a plane-wave basis set, *Comput. Mater. Sci.*, 1996, **6**, 15–50.
22 G. Kresse and J. Furthmüller, Efficient iterative schemes for ab initio total-energy calculations using a plane-wave basis set, *Phys. Rev. B:Condens. Matter Mater. Phys.*, 1996, **54**, 11169–11186.
23 P. E. Blöchl, Projector augmented-wave method, *Phys. Rev. B:Condens. Matter Mater. Phys.*, 1994, **50**, 17953–17979.
24 J. P. Perdew, K. Burke and M. Ernzerhof, Generalized Gradient Approximation Made Simple, *Phys. Rev. Lett.*, 1996, **77**, 3865–3868.
25 H. J. Monkhorst and J. D. Pack, Special points for Brillouin-zone integrations, *Phys. Rev. B*, 1976, **13**, 5188–5192.
26 S. L. Dudarev, G. A. Botton, S. Y. Savrasov, C. J. Humphreys and A. P. Sutton, Electron-energy-loss spectra and the structural stability of nickel oxide: An LSDA + U study, *Phys. Rev. B:Condens. Matter Mater. Phys.*, 1998, **57**, 1505–1509.
27 C. W. M. Castleton, J. Kullgren and K. Hermansson, Tuning LDA + U for electron localization and structure at oxygen vacancies in ceria, *J. Chem. Phys.*, 2007, **127**, 244704.
28 J. Fan, C. Li, J. Zhao, Y. Shan and H. Xu, The Enhancement of Surface Reactivity on CeO_2(111) Mediated by Subsurface Oxygen Vacancies, *J. Phys. Chem. C*, 2016, **120**, 27917–27924.
29 S. Grimme, J. Antony, S. Ehrlich and H. Krieg, A consistent and accurate ab initio parametrization of density functional dispersion correction (DFT-D) for the 94 elements H-Pu, *J. Chem. Phys.*, 2010, **132**, 154104.
30 A. Pedrielli, P. De Vera, P. E. Trevisanutto, N. M. Pugno, R. Garcia-Molina, I. Abril, S. Taioli and M. Dapor, Electronic excitation spectra of cerium oxides: from *ab initio* dielectric response functions to Monte Carlo electron transport simulations, *Phys. Chem. Chem. Phys.*, 2021, **23**, 19173–19187.
31 A. Pfau and K. D. Schierbaum, The electronic structure of stoichiometric and reduced CeO_2 surfaces: an XPS, UPS and HREELS study, *Surf. Sci.*, 1994, **321**, 71–80.
32 T. Skála, F. Šutara, K. C. Prince and V. Matolín, Cerium oxide stoichiometry alteration via Sn deposition: Influence of temperature, *J. Electron Spectrosc. Relat. Phenom.*, 2009, **169**, 20–25.
33 L. Cardenas, C. Molinet-Chinaglia and S. Loridant, Unraveling Ce^{3+} detection at the surface of ceria nanopowders by UPS analysis, *Phys. Chem. Chem. Phys.*, 2022, **24**, 22815–22822.
34 Y. Lykhach, S. M. Kozlov, T. Skála, A. Tovt, V. Stetsovych, N. Tsud, F. Dvořák, V. Johánek, A. Neitzel, J. Mysliveček, S. Fabris, V. Matolín, K. M. Neyman and J. Libuda, Counting electrons on supported nanoparticles, *Nat. Mater.*, 2016, **15**, 284–288.
35 T. Duchoň, M. Aulická, E. F. Schwier, H. Iwasawa, C. Zhao, Y. Xu, K. Veltruská, K. Shimada and V. Matolín, Covalent versus localized nature of 4f electrons in ceria: Resonant angle-resolved photoemission spectroscopy and density functional theory, *Phys. Rev. B*, 2017, **95**, 165124.
36 J. L. F. Da Silva, Stability of the Ce_2O_3 phases: A DFT+U investigation, *Phys. Rev. B:Condens. Matter Mater. Phys.*, 2007, **76**, 193108.
37 L. Zhang, R. Chen, Y. Tu, X. Gong, X. Cao, Q. Xu, Y. Li, B. Ye, Y. Ye and J. Zhu, Revealing the Crystal Facet Effect of Ceria in Pd/CeO_2 Catalysts toward the Selective Oxidation of Benzyl Alcohol, *ACS Catal.*, 2023, **13**, 2202–2213.
38 M. Ziemba, C. Schilling, M. V. Ganduglia-Pirovano and C. Hess, Toward an Atomic-Level Understanding of Ceria-Based Catalysts: When Experiment and Theory Go Hand in Hand, *Acc. Chem. Res.*, 2021, **54**, 2884–2893.
39 X. Zhou, A. Mavridis, M. A. Isaacs, C. Drivas, C. D'Agostino and C. M. A. Parlett, Impact of Ceria Support Morphology on Au Single-Atom Catalysts for Benzyl Alcohol Selective Oxidation, *ChemCatChem*, 2024, **16**, e202301673.
40 J. P. Y. Tan, H. R. Tan, C. Boothroyd, Y. L. Foo, C. B. He and M. Lin, Three-Dimensional Structure of CeO_2 Nanocrystals, *J. Phys. Chem. C*, 2011, **115**, 3544–3551.
41 O. Matz and M. Calatayud, Breaking H_2 with CeO_2: Effect of Surface Termination, *ACS Omega*, 2018, **3**, 16063–16073.
42 B. Hu, K. Sun, Z. Zhuang, Z. Chen, S. Liu, W.-C. Cheong, C. Chen, M. Hu, X. Cao, J. Ma, R. Tu, X. Zheng, H. Xiao, X. Chen, Y. Cui, Q. Peng, C. Chen and Y. Li, Distinct Crystal-Facet-Dependent Behaviors for Single-Atom Palladium-On-Ceria Catalysts: Enhanced Stabilization and Catalytic Properties, *Adv. Mater.*, 2022, **34**, 2107721.
43 D. J. Morgan, Photoelectron spectroscopy of ceria: Reduction, quantification and the myth of the vacancy peak in XPS analysis, *Surf. Interface Anal.*, 2023, **55**, 845–850.
44 Y. Lykhach, V. Johánek, H. A. Aleksandrov, S. M. Kozlov, M. Happel, T. Skála, P. St. Petkov, N. Tsud, G. N. Vayssilov, K. C. Prince, K. M. Neyman, V. Matolín and J. Libuda, Water Chemistry on Model Ceria and Pt/Ceria Catalysts, *J. Phys. Chem. C*, 2012, **116**, 12103–12113.
45 V. Matolín, I. Matolínová, F. Dvořák, V. Johánek, J. Mysliveček, K. C. Prince, T. Skála, O. Stetsovych, N. Tsud, M. Václavů and B. Šmíd, Water interaction with CeO_2(111)/Cu(111) model catalyst surface, *Catal. Today*, 2012, **181**, 124–132.
46 A. I. Stadnichenko, V. V. Muravev, S. V. Koscheev, V. I. Zaikovskii, H. A. Aleksandrov, K. M. Neyman and A. I. Boronin, Study of active surface centers of Pt/CeO_2 catalysts prepared using radio-frequency plasma sputtering technique, *Surf. Sci.*, 2019, **679**, 273–283.
47 Y. Zhu, J. Wang, S. B. Patel, C. Li, A. R. Head, J. A. Boscoboinik and G. Zhou, Tuning the surface reactivity of oxides by peroxide species, *Proc. Natl. Acad. Sci. U. S. A.*, 2023, **120**, e2215189120.
48 T. G. Avval, S. Chatterjee, G. T. Hodges, S. Bahr, P. Dietrich, M. Meyer, A. Thißen and M. R. Linford, Oxygen gas, O2(g), by near-ambient pressure XPS, *Surf. Sci. Spectra*, 2019, **26**, 014021.
49 P. A. Thiel and T. E. Madey, The interaction of water with solid surfaces: Fundamental aspects, *Surf. Sci. Rep.*, 1987, **7**, 211–385.
50 R. Gillen, S. J. Clark and J. Robertson, Nature of the electronic band gap in lanthanide oxides, *Phys. Rev. B:Condens. Matter Mater. Phys.*, 2013, **87**, 125116.

51 C. Li, K. Domen, K. Maruya and T. Onishi, Dioxygen adsorption on well-outgassed and partially reduced cerium oxide studied by FT-IR, *J. Am. Chem. Soc.*, 1989, **111**, 7683–7687.
52 Y. Zhao, B.-T. Teng, X.-D. Wen, Y. Zhao, Q.-P. Chen, L.-H. Zhao and M.-F. Luo, Superoxide and Peroxide Species on CeO_2(111), and Their Oxidation Roles, *J. Phys. Chem. C*, 2012, **116**, 15986–15991.
53 K. K. Chakarova, V. R. Zdravkova, B. S. Karapenchev, D. D. Nihtianova, E. Z. Ivanova, H. A. Aleksandrov, I. Z. Koleva, D. A. Panayotov, M. Y. Mihaylov, G. N. Vayssilov and K. I. Hadjiivanov, Evolution of Ce^{4+} Lewis acidity during dehydroxylation of ceria nanoparticles with different morphology: An integrated FTIR, DFT and HRTEM study, *J. Catal.*, 2024, **433**, 115463.